

Structural basis for recognition of antihistamine drug by human histamine receptor

Received: 23 December 2021

Accepted: 5 October 2022

Published online: 15 October 2022

 Check for updatesXueqian Peng¹, Linlin Yang², Zixuan Liu¹, Siyi Lou¹, Shiliu Mei¹, Meiling Li², Zhong Chen³ & Haitao Zhang^{1,4} ✉

The histamine receptors belong to the G protein-coupled receptor (GPCR) superfamily, and play important roles in the regulation of histamine and other neurotransmitters in the central nervous system, as potential targets for the treatment of neurologic and psychiatric disorders. Here we report the crystal structure of human histamine receptor H₃R bound to an antagonist PF-03654746 at 2.6 Å resolution. Combined with the computational and functional assays, our structure reveals binding modes of the antagonist and allosteric cholesterol. Molecular dynamic simulations and molecular docking of different antihistamines further elucidate the conserved ligand-binding modes. These findings are therefore expected to facilitate the structure-based design of novel antihistamines.

The biogenic amine histamine plays important pathophysiological roles in both the central nervous system (CNS) and periphery tissues, such as allergy, gastric acid secretion, neurotransmission, and immune response¹. The action of histamine is mediated through four subtypes of G protein-coupled receptors (GPCRs), H₁R, H₂R, H₃R, and H₄R². Antagonists of H₁R and H₂R have been clinically used for the treatment of allergies and gastric acid-related diseases, and the H₃R inverse agonist Pitolisant (Wakix[®]) was approved for the treatment of narcolepsy³. While H₄R antagonists are still in the clinical trials for their potential therapeutics in immune-related diseases⁴. Structures of H₁R in complex with the agonist and antagonist have been determined^{5,6}, providing the molecular mechanisms for ligand recognition and facilitating the structure-based design of novel drugs targeting H₁R. However, the molecular mechanisms for ligand recognition with other histamine receptors were still elusive, due to the lacking of the H₂R, H₃R, and H₄R structures.

H₃R is expressed mainly in the brain and acts as an auto- or hetero-receptor in the histaminergic neurons⁷. As an auto-receptor,

H₃R modulates the histamine release by the negative feedback⁸. While, as a hetero-receptor, H₃R regulates the release of various neurotransmitters such as dopamine, γ -aminobutyric acid (GABA), and acetylcholine⁹. It was suggested that H₃R was associated with several physiological progresses such as sleeping and wakefulness, learning and memory, feeding, and cerebral ischemia^{10–12}. Therefore, H₃R is a potential target for the treatment of neurologic and psychiatric disorders, such as sleep disorders, Parkinson's disease, schizophrenia, Alzheimer's disease, and cerebral ischemia^{13,14}. The imidazole antagonist of H₃R showed poor penetration through the blood–brain barrier and unwanted interactions with hepatic cytochrome P450¹⁵. Thus, great efforts have been devoted to the development of non-imidazole H₃R antagonists¹⁵. Here we determine the crystal structure of human H₃R bound to a non-imidazole antagonist PF-03654746 at 2.6 Å resolution. The structure, together with the computational and functional assays, reveals the critical interactions for the ligand binding, as well as the unexpected cholesterol binding at the allosteric site, which could accelerate the structure-based design of novel antihistamines.

¹Hangzhou Institute of Innovative Medicine, Institute of Pharmacology and Toxicology, Zhejiang Province Key Laboratory of Anti-Cancer Drug Research, College of Pharmaceutical Sciences, Zhejiang University, 310058 Hangzhou, Zhejiang, China. ²Department of Pharmacology, School of Basic Medical Sciences, Zhengzhou University, 450052 Zhengzhou, Henan, China. ³Key Laboratory of Neuropharmacology and Translational Medicine of Zhejiang Province, College of Pharmaceutical Sciences, Zhejiang Chinese Medical University, 310053 Hangzhou, Zhejiang, China. ⁴The Second Affiliated Hospital, Zhejiang University School of Medicine, 310009 Hangzhou, Zhejiang, China. ✉e-mail: haitaozhang@zju.edu.cn

Results

Overall structure of H₃R

To obtain the stable human H₃R proteins for structure determination, the flexible regions of the N-terminal residues 1–26, intracellular loop 3 (ICL3) residues 242–346, and C-terminal residues 433–445 were truncated, and a thermostabilized apocytochrome *b*₅₆₂RIL (BRIL) was inserted at the N-terminus. Additionally, a mutation of S121^{3.39}K (superscript indicates residues numbers according to the Ballesteros–Weinstein scheme¹⁶) at the putative allosteric Na⁺ binding site was introduced to improve the homogeneity and thermostability of H₃R as described in several GPCR structures determination^{17–22} (Supplementary Fig. 1b, c). In our calcium mobilization assays, the crystallized construct of H₃R with S121^{3.39}K mutation could be activated by histamine with ~3-fold lower efficacy but inhibited by PF-03654746 with ~18-fold higher efficacy (Supplementary Fig. 2, Supplementary Table 1), which was in consistent with our results that the crystallized H₃R-PF-03654746 proteins showed significantly improved homogeneity and thermostability (Supplementary Fig. 1). The crystal structure of H₃R in complex with the antagonist PF-03654746 was determined at 2.6 Å resolution (Fig. 1, Supplementary Fig. 1, Supplementary Table 3).

The H₃R structure consisted of the canonical seven transmembrane helical bundles (TMs1–7) connected by three extracellular loops (ECLs1–3) and three intracellular loops (ICLs1–3) with an amphipathic helix 8 (Fig. 1a). The ECL2 of H₃R was stabilized by the conserved disulfide bridge between C107^{3.25} and C188^{ECL2}, and the second disulfide bridge was found between C384^{ECL3} and C388^{ECL3} (Fig. 1a, b). Compared with the inactive H₁R structure⁵, the extracellular tips of TM6 and TM7 in H₃R moved inwards by 2.3 and 3.5 Å, respectively (Fig. 1b). Additionally, the first section of ECL2-shifted towards TM3 by 11 Å and extended from the receptor core, otherwise the antagonist PF-03654746 would clash with ECL2 if it adopted a similar conformation to that in H₁R (Fig. 1b). At the intracellular side, the TM6 of H₃R showed an outward movement of

2.8 Å compared to the inactive H₁R, whereas the active H₁R showed the TM6 outward movement of 12 Å (Fig. 1c). Moreover, the ICL2 of H₃R was found to form an additional helix (Fig. 1c, d). Notably, the Y^{3.51} of D^{3.49}–R^{3.50}–Y^{3.51} motif in H₃R was substituted by F133^{3.51}, with the salt bridge formed between D131^{3.49} and R132^{3.50}, which was a key feature of the inactive state of GPCRs²³ (Fig. 1d).

PF-03654746 binding to H₃R

In our H₃R structure, PF-03654746 occupies a shallow pocket at the extracellular side, with clear densities for both the receptor and ligand (Fig. 2a). Although the orthosteric binding pocket of H₃R is relatively shallow, an extended binding pocket (EBP) was found around TMs2/7 and ECL2 in H₃R, compared to other aminergic receptors^{24,25} (Fig. 2a). The ligand-binding pocket of H₃R is constituted by the residues mainly from TMs2/3/6/7 and ECL2 (Fig. 2b). At the extracellular side, the carbonyl and N-ethyl-carboxamide moieties of PF-03654746 extends into the EBP by forming hydrophobic and hydrogen interactions with E395^{7.36} and Y91^{2.61}, respectively (Fig. 2b). In our calcium mobilization assays, the E395^{7.36}A mutant could fully abolish the PF-03654746 inhibition, while the Y91^{2.61}A mutant could significantly decrease the PF-03654746 inhibition by ~46-fold (Supplementary Fig. 3a, Supplementary Table 1). Both Y^{2.61} and E^{7.36} are located in the minor pocket of aminergic GPCRs, which were shown to determine the ligand affinity and selectivity²⁶. Additionally, the 3-fluoro-phenyl moiety of PF-03654746 formed hydrophobic interaction with F193^{ECL2} (Fig. 2b). Mutating F193^{ECL2} to alanine could completely abolish the PF-03654746 inhibition (Supplementary Fig. 3a, Supplementary Table 1). This phenylalanine on ECL2 was suggested to determine the ligand specificity among the aminergic receptors^{27,28}. Moreover, the hydrophobic interaction with PF-03654746 is seen with Y374^{6.51} (Fig. 2b). Mutagenesis of Y374^{6.51}A could fully abolish the PF-03654746 inhibition

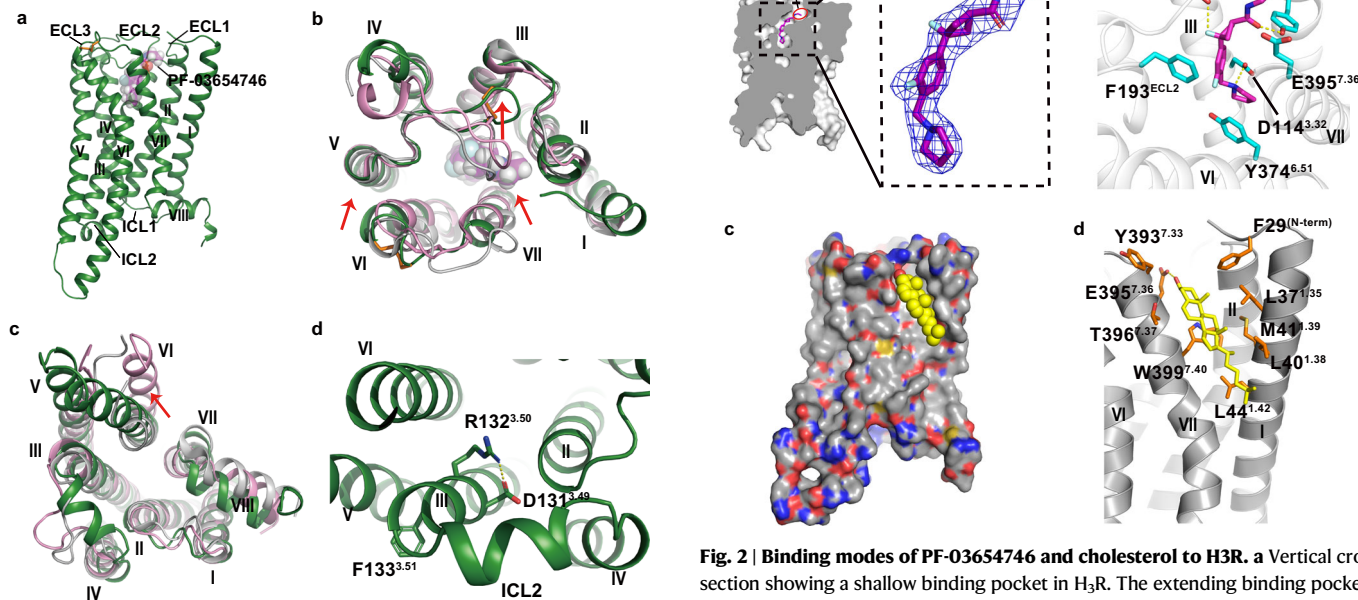


Fig. 2 | Binding modes of PF-03654746 and cholesterol to H₃R. **a** Vertical cross section showing a shallow binding pocket in H₃R. The extending binding pocket (EBP) of H₃R-PF03654746 is shown in a red ellipse. $|2F_o - F_c|$ electron density map for the PF-03654746 contoured at 1.0 σ . **b** Detailed interactions of PF-03654746 in the H₃R ligand-binding pocket. H₃R was shown in gray ribbons, with critical residues for ligand-binding as cyan sticks and PF-03654746 as magenta sticks. Hydrogen bonds were shown as yellow dashed lines. **c** Surface representation of cholesterol-binding site with cholesterol shown in yellow spheres. **d** Detailed interactions of cholesterol with H₃R. Residues critical for cholesterol binding were shown as orange sticks and cholesterol was shown as yellow sticks. The hydrogen bond was shown as yellow dashed lines.

Fig. 1 | Overall structure of H₃R-PF-03654746 complex. **a** Membrane view of H₃R-PF-03654746 structure. H₃R was shown in forest green ribbons. PF-03654746 was shown in a magenta sphere. The disulfide bond was shown as orange sticks. **b, c** Structural comparison of H₃R (forest green) with inactive H₁R (gray, PDB ID: 3RZE) and active H₁R (pink, PDB ID: 7DFL) from extracellular view (**b**) and intracellular view (**c**). **d** Intracellular view showing a salt-bridge interaction (yellow dashed line) between D131^{3.49} and R132^{3.50}. The red arrows indicated movements of TMs5/6 and ECL2 in the H₃R structure compared to the H₁R inactive structure.

(Supplementary Fig. 3a, Supplementary Table 1). Notably, the fluorine atom of 3-fluoro-cyclobutane of PF-03654746 engages a hydrogen bond with C188^{45,50}, and the amine moiety of pyrrolidine of PF-03654746 forms a salt bridge with D114^{3,32} at the bottom of the pocket (Fig. 2b), which is highly conserved in the aminergic receptors²⁸. Surprisingly, both D114^{3,32}A and C188^{45,50}A mutations displayed similar PF-03654746 inhibition on the histamine-induced calcium mobilization compared to the wild-type (Supplementary Fig. 3a, Supplementary Table 1). However, the D114^{3,32}A and C188^{45,50}A mutants showed ~6-fold and ~4-fold reduction of histamine activation, indicating these two residues might be involved in the binding of both histamine and PF-03654746 (Supplementary Fig. 3a, Supplementary Table 1). Indeed, D^{3,32} forms hydrogen bonds with histamine in H₃R⁶.

Cholesterol binding to H₃R

Cholesterol has been observed in many GPCR structures for its regulatory roles^{29–33}, at the classical cholesterol consensus motif (CCM)³⁴, as well as diverse binding sites^{35–40}. In the adrenergic receptor β_2 AR, two cholesterol molecules bound at the CCM stabilizing the receptor conformation³⁴, while two other cholesterol molecules were observed around helix 8 and TMI, modulating the β_2 AR dimerization³⁹. In the histamine receptors, the cholesterol-binding site was not identified previously. In our structure, the electron density of a cholesterol molecule is observed around TMI and TM7 of H₃R (Fig. 2c). Cholesterol forms extensive hydrophobic interactions in the extrahelical pocket consisting of F29^{N-term}, L37^{1,35}, M41^{1,39}, L40^{1,38}, L44^{1,42}, T396^{7,37}, Y393^{7,33}, and W399^{7,40}. Especially, the β -hydroxy head group of cholesterol interacts with E395^{7,36} through hydrogen bonding (Fig. 2d). Notably, E395^{7,36} also participates in the polar interactions with PF-03654736 (Fig. 2b). Our functional assays showed that mutating the negatively charged E395^{7,36} to uncharged alanine or positively charged arginine had little effects on the histamine activation, while completely abolishing the PF-03654746 inhibition, indicating that cholesterol binding to E395^{7,36} might not be critical for agonist binding and H₃R activation, but might potentially affect antagonist binding and H₃R inhibition through an allosteric mode (Supplementary Fig. 3a, Supplementary Table 1).

To investigate the effects of cholesterol binding on H₃R, molecular dynamics (MD) simulations were performed on H₃R/PF-03654746 complex in the presence and absence of the crystal cholesterol molecule. Two systems, H₃R/PF-03654746/cholesterol (hereafter referred to as CHL) and H₃R/PF-03654746 (hereafter referred to as PF), were embedded in the palmitoyl oleoyl phosphatidylcholine (POPC) bilayer with a duration of 2000 ns, respectively, and each system was replicated to perform three independent simulations. A free-energy landscape was built to analyze the conformational changes in six 2- μ s MD trajectories. RMSD_{residues} and RMSD_{PF}, representing the root mean square deviations (RMSD) of orthosteric site residues and that of PF-03654746, respectively, were used as two collective variables of the landscape (Supplementary Fig. 4b). The small value of these parameters means the more approaching to the starting crystal conformation, while the larger value indicates obvious movements for both protein and PF-03654746.

The free-energy landscape showed three main minima corresponding to three states of the complexes: crystal-like state, state 2, and state 3 (Supplementary Fig. 4a). The crystal-like state contained snapshots from simulations CHL1, CHL2, and PF3 and displayed the smallest RMSD_{PF} and RMSD_{residues}, representing the closest conformation to crystal structure. It is associated with the lowest free energy and is therefore the most stable. With larger RMSD_{PF} and RMSD_{residues}, snapshots in simulation CHL3 formed state 2, and complexes from PF1 and PF2 fell into state 3. Both states were different from the crystal conformation and are characterized by higher free-energy values. In the crystal-like state, the PF-03654746-binding geometry was similar to that in the crystal structure, especially in the middle and bottom of the binding pocket (Supplementary Fig. 4a),

where salt bridges with D114^{3,32} and hydrophobic interactions existed in every system. In the EBP, PF-03654746 was not that stable and adopted slightly different conformations, forming hydrogen bonds with Y91^{2,61} in CHL1 and CHL2 systems or with Y94^{2,64} in the PF3 system. Though PF-03654746 maintained the stable salt bridge with D114^{3,32} in state 2, its conformation changed in the middle and external parts of the pocket and only occasionally interacted with A190^{ECL2}. For state 3, PF-03654746 totally lost its binding pose and rarely interacted with D114^{3,32}, resulting in a random orientation in each MD trajectory. It's noteworthy that the cholesterol molecule in CHL3 was not so stable as in CHL1 and CHL2 and eventually dissociated from its binding site at the TMI–TM7 interface (Supplementary Fig. 5a, c), so cholesterol-bound complexes only existed in simulations CHL1 and CHL2, and both of them were stabilized into the crystal-like conformations. Considering that one out of four cholesterol-unbound simulations also reproduced the crystal binding mode of PF-03654746, we came to the conclusion that cholesterol at the TMI–TM7 groove was not very stable and not the determining factor for complex stability, but bound cholesterol facilitated PF-03654746 present in the crystal pose at a higher frequency.

A significant phenomenon observed is that the conserved W399^{7,40} played an essential role in stabilizing the cholesterol binding and ligand–H₃R interactions. W399^{7,40} predominantly maintained the original rotameric state (RI-I, $\chi_1 \approx -80^\circ$ and $\chi_2 \approx 100^\circ$) in CHL1 and CHL2 (Supplementary Fig. 5b), and cholesterol resided stably in its site, forming a parallel π – π stacking with W399^{7,40} (Supplementary Fig. 5a, c). But in the CHL3 simulation, the side chain of W399^{7,40} flipped out of the TMI–TM7 cleft and pointed outward to the lipids at about 400 ns, resulting in a new rotamer conformation (RT-II, $\chi_1 \approx 175^\circ$ and $\chi_2 \approx 100^\circ$) (Supplementary Fig. 5b, d). The side chain flipping reduced π – π stacking and caused a big steric hindrance for the bound cholesterol. As a result, cholesterol gradually dissociated from the cleft (Supplementary Fig. 5a, c). Lacking the stabilization of cholesterol, the side chain of W399^{7,40} turned to another conformation (RT-III) at about 1200 ns, and RMSD_{PF} and RMSD_{residues} in CHL3 greatly increased at the same time (Supplementary Fig. 4b). The observations above predicted that cholesterol regulated the complex dynamics by stabilizing W399^{7,40} in RI-I state. To verify the role of W399^{7,40} in ligand binding, we further analyzed the rotameric states of W399^{7,40} in non-cholesterol system. As expected, W399^{7,40} in PF1 and PF2 underwent a certain conformational change, while W399^{7,40} of PF3 predominantly displayed RI-I state throughout the simulation, which should contribute to the stable conformation of H₃R/PF-03654746 complex obtained in this trajectory (Supplementary Fig. 5f).

To explore how W399^{7,40} influenced the ligand binding, we examined its interactions with surrounding residues in the crystal structure. W399^{7,40} formed T-shape π – π stackings with Y91^{2,61}, which was important for the PF-03654746 binding (Supplementary Fig. 5e). Indeed, mutation of W399^{7,40}A could completely abolish the PF-03654746 inhibition, while had little effects on the histamine activation (Supplementary Fig. 3a, Supplementary Table 1), indicating that cholesterol might affect the PF-03654746 binding mediated by the cholesterol–W399^{7,40}–Y91^{2,61}–PF-03654746 interactions. W399^{7,40} and D114^{3,32} are completely conserved, and W402^{7,43} is highly conserved among monoamine receptors. Experiments have independently indicated the importance of W^{7,40} for the ligand binding in several GPCRs^{41,42}. Therefore, our study provided additional support for this idea and suggested a relevance between cholesterol and the W399^{7,40}–W402^{7,43}–Y91^{2,61} motif.

More importantly, cholesterol facilitated rearrangements of the TMI–TM7 interface and stabilized a polar network of cholesterol–E395^{7,36}–R27^{N-term}. By making extensive hydrophobic contacts with the extrahelical part of TMI and TM7, cholesterol joined TMI and TM7 tightly like a 'glue' and promoted the formation of E395^{7,36}–R27^{N-term} salt bridge (Supplementary Fig. 6a–c). Meanwhile,

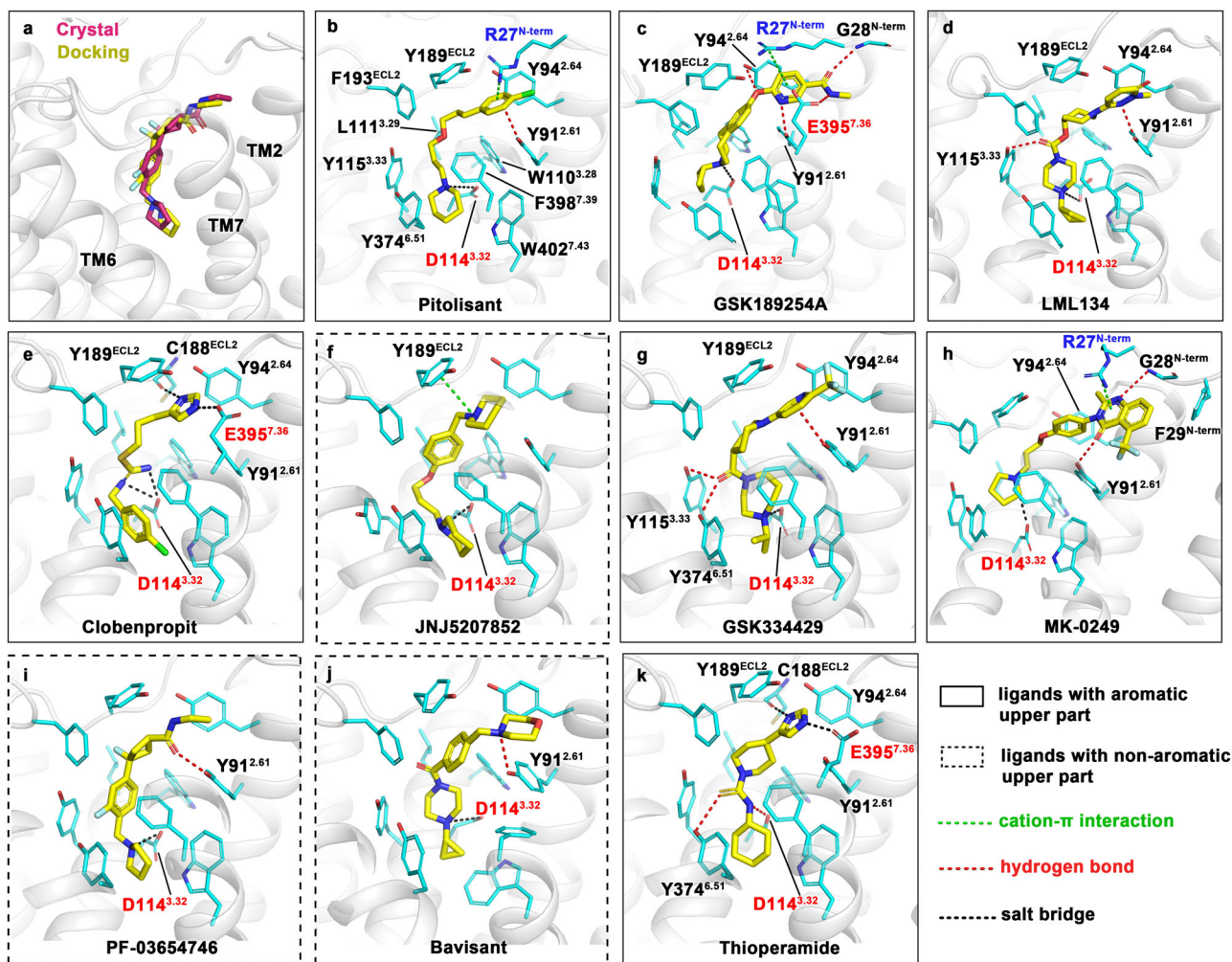


Fig. 3 | Docking results of PF-03654746 and nine different H₃R antagonists. **a** Superimposition of PF-03654746 in the crystal structure (magenta) and the docked pose (yellow). **b–k** Binding modes of 10 H₃R antagonists. The docked ligands were depicted as yellow sticks and arranged according to their K_i values from low to high as shown in Supplementary Table 2. Ligands with an aromatic moiety in the upper part of their binding poses were boxed with solid lines and ligands with non-aromatic upper parts were marked with dash

lines. Interacting residues were presented as cyan sticks. In **b**, all residues involved in interactions were labeled. In **c–k**, only residues forming interactions with the external aromatic moiety or involved in polar contacts were labeled. Charged residues were marked in red (negative) or blue (positive). Polar interactions, including cation- π interactions, hydrogen bonds, and salt bridges, were represented by different colored dash lines, while π - π stackings were not shown.

the hydroxy of cholesterol established a stable hydrogen bond with the carboxyl group of E395^{7,36} in our simulation, as indicated by the time dependences of their distance (Supplementary Fig. 5a). Hence, cholesterol-E395^{7,36}-R27^{N-term} polar network remained in CHL1 and CHL2, like in the crystal structure (Supplementary Fig. 6a). In the cholesterol-unbound simulations, only PF3 possessed the stable E395^{7,36}-R27^{N-term} salt bridge and similar compact conformation in TM1-TM7 interface. As for CHL3, PF1, and PF2, they showed declining stability of TM1 and TM7, as well as the E395^{7,36}-R27^{N-term} interaction (Supplementary Fig. 6b–e), consistent with their unstable complex states. Accordingly, the tight TM1-TM7-N-term contacts seemed to be favorable for ligand binding and cholesterol stabilized this receptor conformation through both hydrophobic and electrostatic interactions.

Conserved binding modes of H₃R antagonists

To explore the binding modes of different H₃R antagonists, molecular docking studies were used to predict the binding conformations of other 9 H₃R antagonists (Fig. 3). PF-03654746 was first redocked into the protein to verify the reliability of the docking simulation, which showed the RMSD < 3.0 Å with the solved crystal

structure (Fig. 3a). All ligands fit well in the binding pocket and all predicted docking scores were lower than -8.4 kcal/mol (Supplementary Table 4), which was inconsistent with the experimental K_i values of these ligands (Fig. 3b–k)^{13,43,44}.

The docking results showed a common binding pose for all ligands. Apart from the conserved salt bridges with D114^{3,32}, docking studies revealed that favorable interactions between the aromatic upper part of ligands and residues in the EBP, as well as strong hydrophobic contacts at the bottom of the pocket, are of great importance for the ligand binding and efficacy. For all ligands, the downward heterocycle was in the hydrophobic pocket constituted by Y115^{3,33}, Y374^{6,51}, F398^{7,39}, and W402^{7,43} (Fig. 3b). In the docked poses, conserved salt bridges were found between D114^{3,32} and protonated nitrogen atoms at the bottom of the binding pocket for each ligand except Thioperamide. As Thioperamide did not get protonated at the equivalent position, it only formed a hydrogen bond with D114^{3,32} (Fig. 3k), which might partly explain its worse inhibitive activity when compared with other antagonists (Supplementary Table 4). The middle part of the ligand was stabilized through hydrophobic interactions with L111^{3,29}, W110^{3,28}, F193^{ECL2}, and Y189^{ECL2} (Fig. 3b), and the middle carbonyl group in GSK334429,

LML134, and the carbothioamide group in Thioperamide formed additional hydrogen bonds with Y374^{6,51} and Y115^{3,33} (Fig. 3d, g, k).

In the EBP, there were two general patterns of receptor–ligand interactions. Except for PF-03654746, JNJ5207852, and Bavisant, the other seven ligands all possess an aromatic moiety in the upper part of their binding poses, which could establish favorable π – π stacking interactions and OH/ π hydrogen bonds with a cluster of aromatic residues in the EBP that involve Y91^{2,61} and Y189^{ECL2}. This was further validated by our functional assays that the Y91^{2,61}A mutant significantly decreased the inhibition of GSK189254A and JNJ5207852 by -25-fold and -23-fold, respectively, and completely abolished the inhibition of Pitolisant (Supplementary Fig. 3b–d, Supplementary Table 2). While, the Y189^{ECL2}A mutant decreased the inhibition of GSK189254A by -88-fold and completely abolished the inhibition of Pitolisant (Supplementary Fig. 3b–d, Supplementary Table 2). On the other hand, ligands without aromatic moiety formed much fewer and weaker interactions in the EBP (Fig. 3f, i, j). Apparently, the extensive interactions benefit ligands binding and support the observation that most of the seven ligands with aromatic external moieties exert better inhibitive activity than ligands with non-aromatic groups (Fig. 3, Supplementary Table 4), highlighting the importance of aromatic rings in this part for H₃R antagonists. Additionally, with larger aromatic groups, GSK189254A and MK-0249 extended to reach the TM1–TM7 interface and even interacted with G28^{N-term}, E395^{7,36}, and F29^{N-term} (Fig. 3c, h). The imidazole moiety in Thioperamide and Clobenpropit also formed polar interactions with C188^{ECL2} and E395^{7,36} in H₃R (Fig. 3e, k), in which the only non-conserved residue was R341^{7,36} in H₄R (Supplementary Table 5), providing a structural basis for Thioperamide with similar affinity in H₃R and H₄R¹. Indeed, the E395^{7,36}A and E395^{7,36}R mutants could fully abolish the inhibition of Thioperamide and Clobenpropit (Supplementary Fig. 3e, f, Supplementary Table 2).

Further analysis suggested hydrophobic interactions at the bottom of the pocket play a role in ligand binding as well. Though JNJ5207852 and Bavisant showed similar contacts in the EBP through a protonated nitrogen atom (Fig. 3f, j), JNJ5207852 displays a much lower K_i value (Supplementary Table 4), which may be the result of stronger hydrophobic packings made by the piperidine of JNJ5207852 than the cyclopropane of Bavisant. This could also be the reason why JNJ5207852 has better activity than GSK334429 and MK-0249 in spite that they formed more contacts in the EBP (Fig. 3f, g, h). It is the same in the case of Clobenpropit and Thioperamide. With identical interactions in the EBP, Clobenpropit not only established more powerful salt bridges with D114^{3,32} as mentioned above but made more hydrophobic contacts through the fluorobenzene moiety at the bottom of the binding site (Fig. 3e, k).

Taken together, a combination of aromatic interactions in the EBP, salt bridges with D114^{3,32} and hydrophobic patterns at the bottom of the pocket stabilized H₃R/antagonist complex. This exquisite binding feature rationalized the ability of Pitolisant, which possesses both a fluorobenzene group in the upper part and piperidine at the other end, to exhibit the best inhibitive activity among all ligands (Fig. 3b, Supplementary Table 4). In summary, the predicted poses of several H₃R antagonists demonstrate a conserved binding feature targeting H₃R, which could facilitate the future structure-based drug design.

Mechanism of H₃R antagonism

Structural comparison of our determined antagonist-bound H₃R structure with the inactive doxepin-bound H₁R⁵ and active histamine-bound H₁R⁶ structures provides an opportunity to visualize how the antagonist inhibits H₃R (Fig. 4a). A notable difference between H₁R and H₃R is the ligand-binding sites, where doxepin and histamine in H₁R bound deeply in the ligand-binding pocket, without interactions with the extracellular part (Fig. 4a). While, in H₃R, PF-03654746 occupies a shallow site near the extracellular part of the pocket, with only the

pyrrolidine adopting a similar position to the primary amino group of doxepin and histamine in H₁R (Fig. 4a). In the active structure of histamine-bound H₁R⁶, three conserved residues D^{3,32}, T^{3,37}, and Y^{6,51} form extensive hydrogen bonds with histamine and pushes TM6 towards TM3 for H₁R activation. In contrast, in the inactive structures of H₁R⁵ and H₃R, neither the inverse agonist doxepin in H₁R nor the antagonist PF-03654746 in H₃R form hydrogen bonds with Y^{6,51} (Fig. 4a). Y374^{6,51} of H₃R forms hydrophobic interaction with PF-03654746 (Fig. 2b), and mutation of Y374^{6,51}A could fully abolish the PF-03654746 inhibition, while showing little effects on histamine activation (Supplementary Fig. 3a, Supplementary Table 1), indicating Y374^{6,51} might be critical for PF-03654746 binding but not histamine binding to H₃R. D114^{3,32} might be an overlapping binding site for both histamine and PF-03654746 since D114^{3,32}A mutant showed similar PF-03654746 inhibition on the histamine-induced calcium mobilization compared to the wild-type, but a -6-fold reduction of histamine activation (Supplementary Fig. 3a, Supplementary Table 1). T119^{3,37} in H₃R forms two intramolecular hydrogen bonds with E206^{5,46}, which is different from T112^{3,37} in H₁R by forming hydrogen bonds with either doxepin or histamine (Fig. 4a). E206^{5,46} of H₃R was suggested to form hydrogen bonds with the nitrogen atom in the imidazole ring of histamine and contribute to the binding of the selective H₃R agonist with a similar imidazole ring^{13,45}, indicating E206^{5,46} might be critical for the H₃R activation.

Additionally, L401^{7,42} forming hydrophobic interaction with PF-03654746 in H₃R corresponding to G457^{7,42} in H₁R, which is likely to hinder the side chain of the toggle switch W371^{6,48} in H₃R from forming a similar conformation in H₁R (Fig. 4a, Supplementary Table 4). In H₃R, the side chain of W371^{6,48} is rotated -90° and exhibits a perpendicular conformation relative to that in the H₁R structures (Fig. 4a, b). Consequently, the extracellular half of TM6 is pushed out by the outward displacement of W371^{6,48} and Y374^{6,51}, thus expanding the ligand-binding pocket; contributing to the intracellular half of TM6 stabilizing an inactive state by forming the intramolecular hydrophobic interaction between W371^{6,48} and F367^{6,44} in the PIF motif. Indeed, the pocket volume of PF-03654746-bound H₃R (calculated by the CASTp 3.0 server⁴⁶) was similar to that of the doxepin-bound inactive H₁R, but increased by -3-fold in comparison with the histamine-bound active H₁R, which is in agreement with the expansion of the extracellular binding pocket in the inactive state of H₁R (Supplementary Fig. 7). Together with the intrahelical salt bridge observed between D^{3,49} and R^{3,50} in the DRY motif, and locked state of Y^{7,53} in the NP^{7,50}xxY^{7,53} motif (Fig. 4d, e), these conformational changes resulted in an inactive state of H₃R in complex with PF-03654746 (Fig. 4a, Supplementary Table 4).

Discussion

H₃R plays a crucial role in controlling the release of histamine and other neurotransmitters, and many studies have shown the therapeutic potentials of H₃R inverse agonists in CNS disorders¹⁰, despite its complex pharmacology¹³. Drug discovery targeting H₃R was hampered by the lack of a three-dimensional structure to elucidate the molecular mechanisms for the ligand binding⁴⁵. In this study, we reported a crystal structure of human H₃R in complex with an antagonist PF-03654746, which was developed for the treatment of CNS diseases. Our structure revealed a ligand-binding mode distinct from that of the antagonist-bound H₁R structure. Additionally, in combination with computational and functional assays, conserved binding modes of H₃R antagonists were identified, highlighting the importance of the residues in the EBP and the hydrophobic contacts at the bottom of the pocket for the ligand binding and efficacy. Especially, a cholesterol-binding site was identified next to the ligand-binding pocket, which might be targeted by the allosteric modulators. Our results are therefore expected to facilitate the structure-based novel antihistamine drug discovery targeting H₃R.

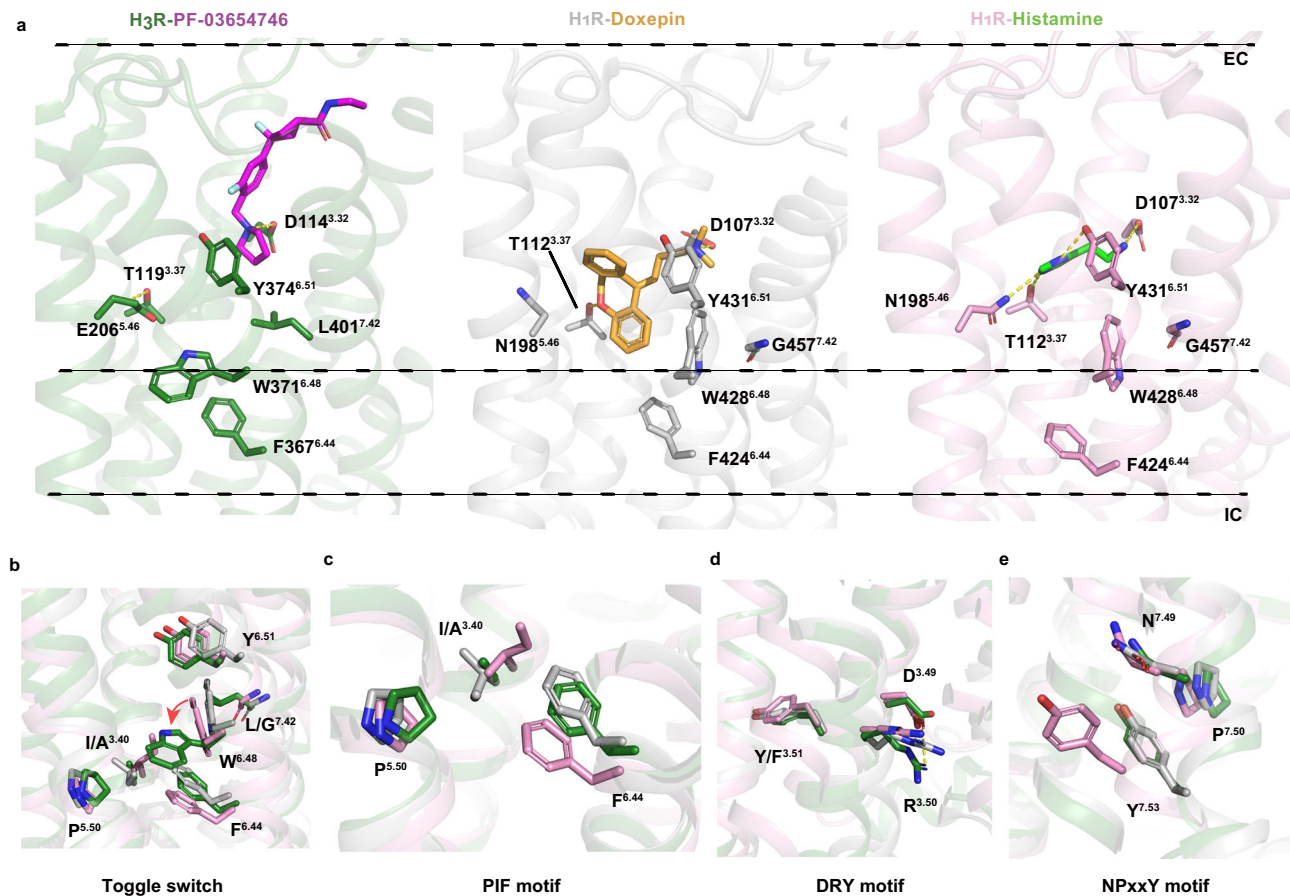


Fig. 4 | Mechanism of H₃R antagonism. **a** Superpositions of the ligand-binding pockets of H₃R–PF-03654746 (H₃R in forest green, PF-03654746 in violet), H₁R–Doxepin (PDB ID: 3RZE, H₁R in gray, Doxepin in yellow), and H₁R–Histamine

(PDB ID: 7DFL, H₁R in pink, Histamine in green) from the membrane view. Structural comparisons of the toggle switch (**b**), PIF motif (**c**), DRY motif (**d**), and NPxxY motif (**e**) with the same colors as **a**.

Methods

Protein engineering for structure determination

The codon-optimized human H₃R gene was cloned into a modified pFastBac1 vector (Invitrogen) containing with N-terminal haemagglutinin (HA) signal sequence followed by a FLAG tag, a 10× His tag, and a tobacco etch virus (TEV) protease cleavage site. The H₃R was modified by introducing S121^{3.39}K mutation to improve the thermostability and expression. To facilitate crystallization, N terminal residues 1–26 were replaced by the thermostabilized apocytochrome *b*₅₆₂RIL (BRIL) from *Escherichia coli* with mutations M7W, H102I, and R106L⁴⁷. The ICL3 residues 242–346 and C terminal residues 433–445 were truncated.

Protein expression and purification

The engineered H₃R protein was expressed in *Spodoptera frugiperda* (*Sf9*) insect cells (Invitrogen) using the Bac-to-Bac Baculovirus Expression System. *Sf9* cells were infected at a density of 2–3 × 10⁶ cells per ml with a multiplicity of infection 5. Cells were harvested 48 h post-infection and stored at –80 °C until use.

Frozen biomass was thawed and disrupted by extensive washing in hypotonic buffer (10 mM HEPES, pH 7.5, 10 mM MgCl₂, 20 mM KCl) containing protease inhibitors (500 μM AEBSF, 1 μM E-64, 1 μM leupeptain, 150 nM aprotinin) and high-osmotic buffer (10 mM HEPES, pH 7.5, 1.0 M NaCl, 10 mM MgCl₂, 20 mM KCl). Purified membranes were resuspended in the hypotonic buffer with the presence of 2 mg/mL iodoacetamide at 4 °C for 30 min, and then solubilized in 50 mM HEPES, pH 7.5, 800 mM NaCl, 0.5% (w/v) n-dodecyl-β-D-maltopyranoside (DDM, Anatrace), 0.1% (w/v) cholesterol hemisuccinate (CHS, Sigma-Aldrich), and 10% (v/v) glycerol for 3 h at 4 °C. After high-speed

centrifugation at 58,000×g for 1 h at 4 °C, the solubilized H₃R proteins in the supernatants were incubated with TALON IMAC resin (TaKaRa) at 4 °C. After incubation overnight, the resin was then washed with 20 column volumes of washing buffer I (50 mM HEPES, pH 7.5, 800 mM NaCl, 10% (v/v) glycerol, 0.1% (w/v) lauryl maltose neopentyl glycol (LMNG, Anatrace), 0.01% (w/v) CHS, 20 mM imidazole), followed by 10 column volumes of wash buffer II (20 mM HEPES, pH 7.5, 500 mM NaCl, 5% (v/v) glycerol, 0.05% (w/v) LMNG, 0.005% (w/v) CHS, 40 mM imidazole). The protein was then eluted in 3 column volumes of elution buffer (10 mM HEPES, pH 7.5, 500 mM NaCl, 5% (v/v) glycerol, 0.01% (w/v) LMNG, 0.001% (w/v) CHS, 250 mM imidazole) and concentrated to 500 μL with a 100 kDa cutoff concentrator (Sartorius). Imidazole was removed by a PD MiniTrap G-25 column (GE Healthcare). Then, the sample was supplemented with 100 μM PF-03654746 and incubated with TEV protease overnight. The TEV protease, cleaved His-tag, and Flag-tag were removed by incubating with TALON IMAC resin (TaKaRa) at 4 °C for 2 h. The purified H₃R–PF-03654746 complex protein was concentrated to ~40 mg/mL with a 100 kDa cutoff concentrator (Sartorius). The protein purity and monodispersity were tested by SDS–PAGE and analytical size-exclusion chromatography (aSEC).

Lipidic cubic phase crystallization

Purified protein was reconstituted in LCP by mixing 40% of protein with 60% of lipid (monoolein and cholesterol, 9:1, w/w) using a syringe lipid mixer. Crystallization trials were performed on a Gryphon LCP robot (ArtRobbins) by dispensing 40 nL of protein-loaded LCP on 96-well glass sandwich plates and overlaying with 800 nL precipitant solution per well. Crystals appeared after 1 day and grew to full size

within 1 week in 0.1 M sodium cacodylate trihydrate, pH 6.4, 90 mM sodium citrate, 34% PEG400, and 0.005% dichloromethane. Crystals were collected directly from LCP using 50 μm micro-loops and flash-frozen in liquid nitrogen.

Data collection and structure determination

The X-ray diffraction data of crystals were collected at the BL18U1 beamline of Shanghai Synchrotron Radiation Facility, using 20 μm \times 20 μm beams for 0.8 s and 1° oscillation per frame with a Pilatus3 6M detector at a wavelength of 1.0000 Å. Diffraction data were processed with HKL3000⁴⁸. Initial phase information was obtained by molecular replacement with CCP4⁴⁹ using M₁R⁵⁰ (PDB ID: 5CXV) and BRIL⁵¹ (PDB ID: 1M6T) as search models. Refinement was performed with COOT⁵² and Phenix⁵³ using $|2F_o - F_c|$ and $|F_o - F_c|$ maps. Pymol (<http://www.pymol.org>) was used to generate all the structural images in this manuscript.

Molecular dynamics simulations

MD simulations on two systems (H₃R/PF-03654746/cholesterol system, H₃R/PF-03654746 system) were performed. Based on the crystal structure, we first built a complex model including H₃R, PF-03654746, and cholesterol. BRIL in the crystal structure was removed and the S121K mutation was mutated back to serine. To investigate the influence of cholesterol, we removed the cholesterol molecule to build a complex model only including H₃R and PF-03654746. These models were separately placed into a 110 Å \times 110 Å palmitoyl oleoyl phosphatidylcholine (POPC) bilayer and the lipids located within 1 Å of the receptor were removed. Both systems were solvated in a box (110 Å \times 110 Å \times 110 Å) with TIP3P water molecules and 0.15 M NaCl. Each system was replicated to perform three independent simulations and each of the three simulations was run up to 2- μs .

MD simulations were carried out with GROMACS 2020⁵⁴ with an isothermal-isobaric (NPT) ensemble and periodic boundary conditions. The CHARMM36-CMAP force field⁵⁵ was applied for protein, POPC phospholipids, cholesterol, ions, and water molecules. Ligand parameters were adapted from the CHARMM Generalized Force Field (CGenFF)^{56,57}. For each system, stepwise energy minimizations were first performed to relieve unfavorable contacts with positional restraints imposed on i/protein, lipids, ligand, and cholesterol, ii/protein, ligand, and cholesterol, iii/mainchain atoms of protein, ligand, and cholesterol, iv/C α atoms of protein, ligand, and cholesterol, v/no atoms. Subsequently, three parallel 50-ns equilibrations MD runs in the NPT ensemble were performed for each system with positional restraints applied in the same order as that in the energy minimization. During the equilibration, temperature and pressure were controlled using the v-rescale method⁵⁸ and the Berendsen barostat⁵⁹, respectively. After equilibration, a 2- μs production run was carried out for each simulation. SETTLE constraints⁶⁰ and LINCS constraints⁶¹ were applied to the hydrogen-involved covalent bonds in water molecules and in other molecules, respectively, and the time step was set to 2 fs. Electrostatic interactions were calculated with the particle-mesh Ewald (PME) algorithm⁶² with a real-space cutoff of 1.0 nm. The temperature was maintained at 310 K using the v-rescale method⁵⁸ and the pressure was kept constant at 1 bar by semi-isotropic coupling to a Parrinello–Rahman barostat⁶³ with $\tau_p = 2.5$ ps and compressibility of 4.5×10^{-5} bar. Analysis of simulation data was conducted using PyMOL (<http://www.pymol.org>), tools implemented in GROMACS 2020, and in-house scripts.

Molecular docking

To investigate the interacting patterns between antagonists and H₃R, we performed flexible molecular docking studies using AutoDock 4⁶⁴. The crystal structure of H₃R reported here was used as the receptor and structures of 10 antagonists downloaded from the PubChem database were used as ligands. The receptor and ligands were

respectively prepared by AutoDockTools to produce the corresponding low-energy three-dimensional conformation and the correct ionization state (pH 7.0). A 3D docking grid centered on PF-03654746 in the crystal structure was generated and residues around the pocket were treated as flexible. Then the processed antagonists were docked into the binding pocket of H₃R, outputting the top 10 conformations for each ligand. The most reliable binding poses were selected according to the interaction energy and visual inspection. All results were analyzed and visualized using PyMOL (<http://www.pymol.org>).

Calcium mobilization assays

Calcium flux was performed as described in our previous studies. Briefly, CHO cells were co-transfected with wild-type or mutant H₃R and G_{q15} using Lipofectamine 2000 according to the manufacturer's manual. Transfected cells were seeded into a 96-well flat clear bottom black plate with a density of 25,000 cells per well and cultured overnight. Subsequently, cells were loaded with calcium dye solution from Calcium 5 assay kit (Molecular Devices) in Hanks' balanced salt solution (20 mM HEPES, 2.5 mM probenecid in HBSS), and incubated at 37 °C for 45 min. Various concentrations of compounds were dispensed into the wells via a Flexstation III instrument (Molecular Devices). The intracellular calcium flux was detected immediately using the Flexstation III instrument (excitation at 485 nm, emission at 525 nm). Data were representative of three independent experiments and analyzed using GraphPad Prism 9.3.1.

Reporting summary

Further information on research design is available in the Nature Research Reporting Summary linked to this article.

Data availability

The data that support this study are available from the corresponding author upon reasonable request. The structural data generated in this study have been deposited in the Protein Data Bank (<http://www.pdb.org/>) under accession code 7F61. The other data generated in this study are provided in the Supplementary Information and Source Data file. Source data are provided with this paper.

References

1. Panula, P. et al. International union of basic and clinical pharmacology. XCVIII. Histamine receptors. *Pharm. Rev.* **67**, 601–655 (2015).
2. Haas, H. & Panula, P. The role of histamine and the tuberomammillary nucleus in the nervous system. *Nat. Rev. Neurosci.* **4**, 121–130 (2003).
3. Panula, P. Histamine receptors, agonists, and antagonists in health and disease. *Handb. Clin. Neurol.* **180**, 377–387 (2021).
4. Tiligada, E. & Ennis, M. Histamine pharmacology: from Sir Henry Dale to the 21st century. *Br. J. Pharm.* **177**, 469–489 (2020).
5. Shimamura, T. et al. Structure of the human histamine H1 receptor complex with doxepin. *Nature* **475**, 65–70 (2011).
6. Xia, R. et al. Cryo-EM structure of the human histamine H(1) receptor/G(q) complex. *Nat. Commun.* **12**, 2086 (2021).
7. Nuutinen, S. & Panula, P. Histamine in neurotransmission and brain diseases. *Adv. Exp. Med. Biol.* **709**, 95–107 (2010).
8. Arrang, J. M., Garbarg, M. & Schwartz, J. C. Auto-inhibition of brain histamine release mediated by a novel class (H3) of histamine receptor. *Nature* **302**, 832–837 (1983).
9. Haas, H. L., Sergeeva, O. A. & Selbach, O. Histamine in the nervous system. *Physiol. Rev.* **88**, 1183–1241 (2008).
10. Schlicker, E. & Kathmann, M. Role of the histamine H(3) receptor in the central nervous system. *Handb. Exp. Pharm.* **241**, 277–299 (2017).
11. Passani, M. B., Lin, J. S., Hancock, A., Crochet, S. & Blandina, P. The histamine H3 receptor as a novel therapeutic target for cognitive and sleep disorders. *Trends Pharm. Sci.* **25**, 618–625 (2004).

12. Yan, H. et al. Histamine H3 receptors aggravate cerebral ischaemic injury by histamine-independent mechanisms. *Nat. Commun.* **5**, 3334 (2014).
13. Nieto-Alamilla, G., Márquez-Gómez, R., García-Gálvez, A. M., Morales-Figueroa, G. E. & Arias-Montaño, J. A. The histamine H3 receptor: structure, pharmacology, and function. *Mol. Pharm.* **90**, 649–673 (2016).
14. Hu, W. & Chen, Z. The roles of histamine and its receptor ligands in central nervous system disorders: an update. *Pharm. Ther.* **175**, 116–132 (2017).
15. Berlin, M., Boyce, C. W. & Ruiz Mde, L. Histamine H3 receptor as a drug discovery target. *J. Med. Chem.* **54**, 26–53 (2011).
16. Ballesteros, J. A. & Weinstein, H. Integrated methods for the construction of three-dimensional models and computational probing of structure-function relations in G protein-coupled receptors. *Methods Neurosci.* **25**, 366–428 (1995).
17. Toyoda, Y. et al. Ligand binding to human prostaglandin E receptor EP(4) at the lipid-bilayer interface. *Nat. Chem. Biol.* **15**, 18–26 (2019).
18. Kimura, K. T. et al. Structures of the 5-HT(2A) receptor in complex with the antipsychotics risperidone and zotepine. *Nat. Struct. Mol. Biol.* **26**, 121–128 (2019).
19. Shao, Z. et al. Structure of an allosteric modulator bound to the CB1 cannabinoid receptor. *Nat. Chem. Biol.* **15**, 1199–1205 (2019).
20. Yan, W. et al. Structure of the human gonadotropin-releasing hormone receptor GnRH1R reveals an unusual ligand binding mode. *Nat. Commun.* **11**, 5287 (2020).
21. Im, D. et al. Structure of the dopamine D(2) receptor in complex with the antipsychotic drug spiperone. *Nat. Commun.* **11**, 6442 (2020).
22. Qin, J. et al. Molecular mechanism of agonism and inverse agonism in ghrelin receptor. *Nat. Commun.* **13**, 300 (2022).
23. Palczewski, K. et al. Crystal structure of rhodopsin: a G protein-coupled receptor. *Science* **289**, 739–745 (2000).
24. Chen, X. et al. Molecular mechanism for ligand recognition and subtype selectivity of $\alpha(2C)$ adrenergic receptor. *Cell Rep.* **29**, 2936–2943.e2934 (2019).
25. Qu, L. et al. Structural basis of the diversity of adrenergic receptors. *Cell Rep.* **29**, 2929–2935.e2924 (2019).
26. Kooistra, A. J., Kuhne, S., de Esch, I. J., Leurs, R. & de Graaf, C. A structural chemogenomics analysis of aminergic GPCRs: lessons for histamine receptor ligand design. *Br. J. Pharm.* **170**, 101–126 (2013).
27. Michino, M. et al. What can crystal structures of aminergic receptors tell us about designing subtype-selective ligands? *Pharm. Rev.* **67**, 198–213 (2015).
28. Vass, M. et al. Aminergic GPCR-ligand interactions: a chemical and structural map of receptor mutation data. *J. Med. Chem.* **62**, 3784–3839 (2019).
29. Yao, Z. & Kobilka, B. Using synthetic lipids to stabilize purified beta2 adrenoceptor in detergent micelles. *Anal. Biochem.* **343**, 344–346 (2005).
30. Muth, S., Fries, A. & Gimpl, G. Cholesterol-induced conformational changes in the oxytocin receptor. *Biochem. J.* **437**, 541–553 (2011).
31. Qiu, Y., Wang, Y., Law, P. Y., Chen, H. Z. & Loh, H. H. Cholesterol regulates micro-opioid receptor-induced beta-arrestin 2 translocation to membrane lipid rafts. *Mol. Pharm.* **80**, 210–218 (2011).
32. Taghon, G. J., Rowe, J. B., Kapolka, N. J. & Isom, D. G. Predictable cholesterol binding sites in GPCRs lack consensus motifs. *Structure* **29**, 499–506.e493 (2021).
33. Duncan, A. L., Song, W. & Sansom, M. S. P. Lipid-dependent regulation of ion channels and G protein-coupled receptors: insights from structures and simulations. *Annu. Rev. Pharm. Toxicol.* **60**, 31–50 (2020).
34. Hanson, M. A. et al. A specific cholesterol binding site is established by the 2.8 Å structure of the human beta2-adrenergic receptor. *Structure* **16**, 897–905 (2008).
35. Jazayeri, A. et al. Extra-helical binding site of a glucagon receptor antagonist. *Nature* **533**, 274–277 (2016).
36. Song, G. et al. Human GLP-1 receptor transmembrane domain structure in complex with allosteric modulators. *Nature* **546**, 312–315 (2017).
37. Zhang, Y. et al. Cryo-EM structure of the activated GLP-1 receptor in complex with a G protein. *Nature* **546**, 248–253 (2017).
38. Lu, J. et al. Structural basis for the cooperative allosteric activation of the free fatty acid receptor GPR40. *Nat. Struct. Mol. Biol.* **24**, 570–577 (2017).
39. Cherezov, V. et al. High-resolution crystal structure of an engineered human beta2-adrenergic G protein-coupled receptor. *Science* **318**, 1258–1265 (2007).
40. Zhang, D. et al. Two disparate ligand-binding sites in the human P2Y1 receptor. *Nature* **520**, 317–321 (2015).
41. Roth, B. L., Shoham, M., Choudhary, M. S. & Khan, N. Identification of conserved aromatic residues essential for agonist binding and second messenger production at 5-hydroxytryptamine2A receptors. *Mol. Pharmacol.* **52**, 259–266 (1997).
42. Rivail, L. et al. New insights into the human 5-HT4 receptor binding site: exploration of a hydrophobic pocket. *Br. J. Pharm.* **143**, 361–370 (2004).
43. Troxler, T. et al. The discovery of LML134, a histamine H3 receptor inverse agonist for the clinical treatment of excessive sleep disorders. *ChemMedChem* **14**, 1238–1247 (2019).
44. Leurs, R., Vischer, H. F., Wijnmans, M. & de Esch, I. J. En route to new blockbuster anti-histamines: surveying the offspring of the expanding histamine receptor family. *Trends Pharm. Sci.* **32**, 250–257 (2011).
45. Kiss, R. & Keserü, G. M. Structure-based discovery and binding site analysis of histamine receptor ligands. *Expert Opin. Drug Discov.* **11**, 1165–1185 (2016).
46. Tian, W., Chen, C., Lei, X., Zhao, J. & Liang, J. CASTp 3.0: computed atlas of surface topography of proteins. *Nucleic Acids Res.* **46**, W363–w367 (2018).
47. Chun, E. et al. Fusion partner toolchest for the stabilization and crystallization of G protein-coupled receptors. *Structure* **20**, 967–976 (2012).
48. Minor, W., Cymborowski, M., Otwinowski, Z. & Chruszcz, M. HKL-3000: the integration of data reduction and structure solution—from diffraction images to an initial model in minutes. *Acta Crystallogr. D Biol. Crystallogr.* **62**, 859–866 (2006).
49. Usón, I., Ballard, C. C., Keegan, R. M. & Read, R. J. Integrated, rational molecular replacement. *Acta Crystallogr. D Struct. Biol.* **77**, 129–130 (2021).
50. Thal, D. M. et al. Crystal structures of the M1 and M4 muscarinic acetylcholine receptors. *Nature* **531**, 335–340 (2016).
51. Chu, R. et al. Redesign of a four-helix bundle protein by phage display coupled with proteolysis and structural characterization by NMR and X-ray crystallography. *J. Mol. Biol.* **323**, 253–262 (2002).
52. Emsley, P., Lohkamp, B., Scott, W. G. & Cowtan, K. Features and development of Coot. *Acta Crystallogr. D Biol. Crystallogr.* **66**, 486–501 (2010).
53. Adams, P. D. et al. PHENIX: a comprehensive Python-based system for macromolecular structure solution. *Acta Crystallogr. D Biol. Crystallogr.* **66**, 213–221 (2010).
54. Abraham, M. J. et al. GROMACS: high performance molecular simulations through multi-level parallelism from laptops to supercomputers. *SoftwareX* **1–2**, 19–25 (2015).
55. Huang, J. & MacKerell, A. D. Jr. CHARMM36 all-atom additive protein force field: validation based on comparison to NMR data. *J. Comput. Chem.* **34**, 2135–2145 (2013).
56. Vanommeslaeghe, K. & MacKerell, A. D. Automation of the CHARMM General Force Field (CGenFF) I: bond perception and atom typing. *J. Chem. Inf. Model.* **52**, 3144–3154 (2012).

57. Vanommeslaeghe, K., Raman, E. P. & MacKerell, A. D. Automation of the CHARMM General Force Field (CGenFF) II: assignment of bonded parameters and partial atomic charges. *J. Chem. Inf. Model.* **52**, 3155–3168 (2012).
58. Bussi, G., Donadio, D. & Parrinello, M. Canonical sampling through velocity rescaling. *J. Chem. Phys.* **126**, 014101 (2007). <https://doi.org/10.1063/1.2408420>.
59. Berendsen, H. J. C., Postma, J. P. M., Vangunsteren, W. F., Dinola, A. & Haak, J. R. Molecular-dynamics with coupling to an external bath. *J. Chem. Phys.* **81**, 3684–3690 (1984).
60. Miyamoto, S. & Kollman, P. A. Settle—an analytical version of the shake and rattle algorithm for rigid water models. *J. Comput. Chem.* **13**, 952–962 (1992).
61. Hess, B., Bekker, H., Berendsen, H. J. C. & Fraaije, J. G. E. M. LINCS: a linear constraint solver for molecular simulations. *J. Comput. Chem.* **18**, 1463–1472 (1997).
62. Essmann, U. et al. A smooth particle mesh Ewald method. *J. Chem. Phys.* **103**, 8577–8593 (1995).
63. Parrinello, M. & Rahman, A. Polymorphic transitions in single-crystals—a new molecular-dynamics method. *J. Appl. Phys.* **52**, 7182–7190 (1981).
64. Morris, G. M. et al. AutoDock4 and AutoDockTools4: automated docking with selective receptor flexibility. *J. Comput. Chem.* **30**, 2785–2791 (2009).

Acknowledgements

H.Z. is supported by the National Key R&D Program of China (2018YFA0508100), the National Natural Science Foundation of China (81722044, 91753115, 21778049, 81861148018), and the National Science and Technology Major Project of China (2018ZX09711002). We thank W.Q., Q.X., and other staff from the BL18U1 beamline of the National Facility for Protein Science in Shanghai (NFPS) at the Shanghai Synchrotron Radiation Facility, for assistance during data collection. We thank W.L. and M.L. from Shanghai Yuyao Biotech Ltd. for their assistance on the calcium mobilization assays.

Author contributions

X.P. designed, expressed, purified, and crystallized the protein, collected the X-ray diffraction data. L.Y. and M.L. performed the computational assays. Z.L., S.L., and S.M. assisted in protein expression, purification, and crystallization. Z.C. supervised the functional assays.

H.Z. conceived and supervised the project, and determined the structures. X.P., L.Y., Z.C., and H.Z. wrote the manuscript with input from all other authors.

Competing interests

The authors declare no competing interests.

Additional information

Supplementary information The online version contains supplementary material available at <https://doi.org/10.1038/s41467-022-33880-y>.

Correspondence and requests for materials should be addressed to Haitao Zhang.

Peer review information *Nature Communications* thanks Giovanni Bottegioni, So Iwata and the other, anonymous, reviewer(s) for their contribution to the peer review of this work. Peer reviewer reports are available.

Reprints and permission information is available at <http://www.nature.com/reprints>

Publisher's note Springer Nature remains neutral with regard to jurisdictional claims in published maps and institutional affiliations.

Open Access This article is licensed under a Creative Commons Attribution 4.0 International License, which permits use, sharing, adaptation, distribution and reproduction in any medium or format, as long as you give appropriate credit to the original author(s) and the source, provide a link to the Creative Commons license, and indicate if changes were made. The images or other third party material in this article are included in the article's Creative Commons license, unless indicated otherwise in a credit line to the material. If material is not included in the article's Creative Commons license and your intended use is not permitted by statutory regulation or exceeds the permitted use, you will need to obtain permission directly from the copyright holder. To view a copy of this license, visit <http://creativecommons.org/licenses/by/4.0/>.

© The Author(s) 2022